PCCP

How to Reprogram the Excitonic Properties and Solid–State Morphologies of π-Conjugated Supramolecular Polymers

Journal:	*Physical Chemistry Chemical Physics*
Manuscript ID	CP-ART-09-2020-004819.R1
Article Type:	Paper
Date Submitted by the Author:	01-Dec-2020
Complete List of Authors:	Liu, Kaixuan; University of Miami Paulino, Victor; University of Miami Mukhopadhyay, Arindam; University of Miami Bernard, Brianna; University of Miami Kumbhar, Amar; University of North Carolina Liu, Chuan; University of Miami Olivier, Jean-Hubert; University of Miami

SCHOLARONE™
Manuscripts

How to Reprogram the Excitonic Properties and Solid-State Morphologies of π-Conjugated Supramolecular Polymers

Kaixuan Liu,[a] Victor Paulino,[a] Arindam Mukhopadhyay,[a] Brianna Bernard,[a] Amar Kumbhar,[b] Chuan Liu,[a] and Jean-Hubert Olivier[a,*]

The development of supramolecular tools to modulate the excitonic properties of non-covalent assemblies paves the way to engineer new classes of semicondcuting materials relevant to flexible electronics. While controlling the assembly pathways of organic chromophores enables the formation of J-like and H-like aggregates, strategies to tailor the excitonic properties of pre-assembled aggregates through post-modification are scarce. In the present contribution, we combine supramolecular chemistry with redox chemistry to modulate the excitonic properties and solid-state morphologies of aggregates built from stacks of water-soluble perylene diimide building blocks. The n-doping of initially formed aggregates in an aqueous medium is shown to produce π-anion stacks which spectroscopic properties unveil a non-negligible degree of electron-electron interactions. Oxidation of the n-doped intermediates produces metastable aggregates where free exciton bandwidths increase as a function of time. Kinetic data analysis reveals that the dynamic increase of free exciton bandwidth is associated with the formation of superstructures constructed by means of a nucleation-growth mechanism. By designing different redox-assisted assembly pathways, we highlight that the sacrificial electron donor plays a non-innocent role in regulating the structure-function properties of the final superstructures. Furthermore, supramolecular architectures formed via a nucleation-growth mechanism evolve into ribbon-like and fiber-like materials in the solid-state, as characterized by SEM and HRTEM. Through a combination of ground-state electronic absorption spectroscopy, electrochemistry, spectroelectrochemistry, microscopy, and modeling, we show that redox-assisted assembly provides a means to reprogram the structure-function properties of pre-assembled aggregates.

Introduction

Molecular aggregates that feature stacks of π-conjugated building blocks (π-stacks) are important classes of semiconducting materials relevant to organic electronics, spintronics, and solar energy capture, conversion, and storage.[1-10] Knowledge acquired over the last few decades has unambiguously underscored the critical role played by molecular order in dictating the linear and non-linear optical properties in addition to the exciton, charge and spin transport properties of organic nanoscale compositions.[11-16] For example, while delocalized charge transfer excitons have been shown to facilitate the formation of free charge carriers in organic solar cells, their formation is contingent upon the existence of strongly interacting frontier molecular orbitals and is intimately related to the conformation of molecular aggregates at the nanoscale dimension.[17, 18]

The pioneering theoretical studies by Bredas, Ratner, Spano, and others have highlighted the importance of interchromophore electronic coupling in non-covalent π-conjugated assemblies and the extent to which it can be leveraged to modulate the (opto)electronic properties of organic semiconducting materials.[19-25] From a theoretical perspective, maximizing the frontier molecular orbital overlap between adjacent π-conjugated cores paves the way to increase the electronic coupling between chromophores, but it requires the formation of a parallel stack geometry (co-facial) that is associated with experimental limitation. In this regard, attractive electrostatic and dispersion energies are well-recognized parameters that regulate the conformation of supramolecular constructs and, consequently, their functions.[26, 27] In solvated π-stacks, also coined π-conjugated supramolecular polymers (SPs), complex interplays of hydrophobic and quadrupole-quadrupole interactions among π-conjugated units parametrize the geometries of these non-covalent assemblies favoring the formation of slipped stack geometries.[28, 29] Consequently, the magnitude with which frontier molecular orbitals overlaps is intimately correlated to non-covalent interactions.

The formation of π-conjugated SPs, in solution, traditionally relies on the assembly of building blocks enforced by a change of temperature, a perturbation of solvent dielectric by the addition of a "bad" solvent, an increase of ionic strength, increase of building block concentration, or a perturbation of pH conditions.[30-33] Exploiting these methods, seminal studies

[a.] Department of Chemistry, The University of Miami, 1301 Memorial Drive, Cox Science Building, Coral Gables, FL 33146 (USA)

[b.] Chapel Hill Analytical and Nanofabrication Laboratory, Department of Applied Physical Sciences, University of North Carolina, 243 Chapman Hall, Chapel Hill, NC 27599
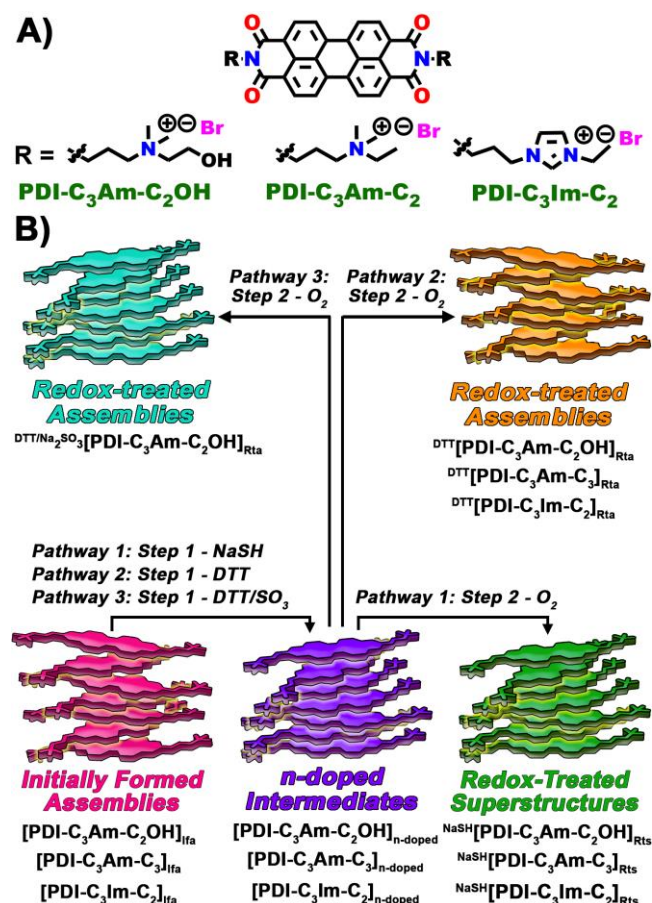
Scheme 1. The redox-assisted assembly processes of the three PDI building blocks shown in (A) are elucidated exploiting the three pathways delineated in (B). (DTT = dithiothreitol).

have demonstrated that pathway-dependent self-assembly processes can provide new opportunities to tune the photophysical properties of molecular aggregates built from perylene diimide (PDI), porphinato(metal), and other π-conjugated building blocks.[34-39] Controlling the assembly pathways to selectively form H- and J-like aggregates from unique building blocks, establishes new principles to modulate interchromophore interactions and, consequently, excitonic coupling.[40, 41] While these studies undoubtedly deliver important guidelines, they are confined to the transformation of one type of aggregate to another, and additional (supra)molecular tools are currently lacking to, for example, optimize the excitonic properties of a specific type of aggregate.

The combination of redox chemistry and supramolecular chemistry can deliver new tools to modulate the structure-function relationships of pre-assembled, non-covalent constructs. Only a handful of studies have demonstrated that the n-doping of well-defined, π-conjugated SPs initiates the formation of kinetically trapped states equipped with enticing optoelectronic properties.[42, 43] Recently, we have reported that the redox-assisted assembly of perylenediimide (PDI)-derived supramolecular polymers enables the formation of H-like

aggregates characterized by a substantial increase of the free exciton bandwidth (Ex_{BW}) when compared to that recorded for the parent assembly.[44] We demonstrated that the n-doped intermediates open a new pathway in the assembly free energy landscape and hold the key to increase the excitonic properties in supramolecular polymers. Herein, we establish novel insights into the parameters governing the structure-function relationships of PDI-derived H-like aggregates in an aqueous medium. After characterizing the electronic structures of the n-doped aggregates using a combination of cyclic voltammetry, spectroelectrochemistry and reductive titration experiments, we unveil that the increase of Ex_{BW} observed in redox-treated superstructures is the product of a dynamic process which not only requires the formation of n-doped intermediates, but also depends on the sacrificial electron donor.

To deliver a general understanding of the synergistic role played by the building block structure and the chemical reductant employed, we engineered the three PDI cores shown in Scheme 1A. While each of the PDI units feature two cationic functional groups placed at an equal distance from the aromatic core by a propyl linker, these building blocks differ in: 1) the structure of the peripheral cationic groups (ammonium and imidazolium), and 2) the terminal side chains which are expected to equip the initial formed assemblies with a more hydrophilic character in [**PDI-C₃Am-C₂OH**]$_{lfa}$, and hydrophobic characters in [**PDI-C₃Am-C₃**]$_{lfa}$ and [**PDI-C₃Im-C₂**]$_{lfa}$ constructs. After elucidating the thermodynamic parameters that govern the assembly of these building blocks using a solvent-dependent equilibrium model, the redox-assisted assembly processes using the three different pathways shown in Scheme1B are scrutinized and reveal that the sacrificial electron donor exploited to produce the n-doped intermediates is involved in the increase of Ex_{BW} bandwidth observed in the final redox-treated superstructures. Furthermore, a systematic investigation of the solid-state morphologies of the assemblies, as a function of the redox-assisted assembly pathway taken, highlights that Pathway 1 enables the formation of hierarchical mesoscale objects with morphologies that are dependent on building block structural attributes.

Results and Discussion

Supramolecular Polymerization Parameters

Solvent-dependent aggregation studies reveal that an isodesmic supramolecular polymerization mechanism regulates the formation of the [**PDI-C₃Am-C₂OH**]$_{lfa}$, [**PDI-C₃Am-C₃**]$_{lfa}$, and [**PDI-C₃Im-C₂**]$_{lfa}$ assemblies in an aqueous medium. Fig. 1A, S1A and S2A chronicle the spectral evolution, as a function of solvent composition, of the **PDI-C₃Am-C₂OH, PDI-C₃Am-C₃,** and **PDI-C₃Im-C₂** building blocks, respectively. In pure water, the ratio of the 0-1 and 0-0 vibronic transitions centered at 500 and 542 nm is below one for the representative **PDI-C₃Am-C₂OH** unit shown in Fig. 1A; the **PDI-C₃Am-C₃** and **PDI-C₃Im-C₂** platforms share similar spectral properties (Fig. S1and S2). These well-established spectroscopic signatures indicate that the [**PDI-C₃Am-C₂OH**]$_{lfa}$, [**PDI-C₃Am-C₃**]$_{lfa}$, and [**PDI-C₃Im-C₂**]$_{lfa}$ building
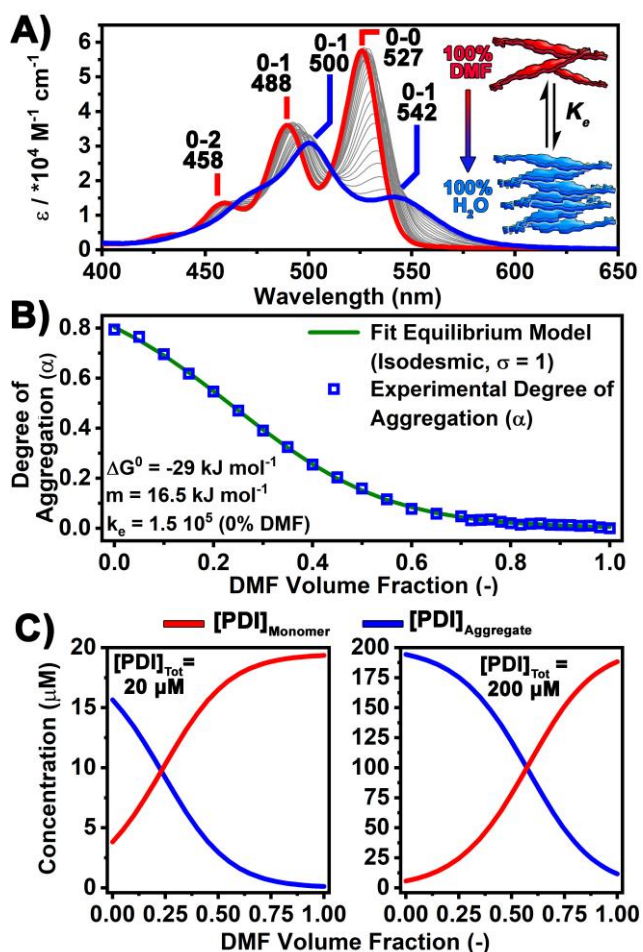
Fig. 1. (A) Solvent-dependent UV-vis spectra of a 20 μM solution of the representative **PDI-C$_3$Am-C$_2$OH** building block in water upon the addition of DMF. (B) Experimental degree of aggregation (empty blue square) as a function of DMF volume fraction. The solid green line represents the best fit using the equilibrium model detailed in the supporting information. Correction factor p used is 1.25. (C) Evolution of the concentration of the free monomer ([PDI]$_{Monomer}$) and the monomers that construct the aggregates ([PDI]$_{Aggregate}$).

blocks exist under an aggregated state best described as H-like aggregates. We have previously shown that PDI-derived building blocks sharing related structural attributes engender the formation of H-like aggregate in water.[45] The addition of a good solvent (DMF) to a solution of PDI aggregates solvated in a poor solvent (H$_2$O) is accompanied with a drastic change of spectroscopic features reminiscent to the formation of individualized building blocks. Fig. 1A highlights the simultaneous rise and hypsochromic shifts of the 0-0 and 0-1 vibronic transitions in addition to an inversion of the 0-0 and 0-1 ratio reaching 1.5 in pure DMF. Furthermore, in pure DMF, the 0-0, 0-1 and 0-2 vibronic transitions are consistently separated by 180 meV (1452 cm^{-1}, aromatic C=C bond stretching), an additional hallmark of molecularly dissolved PDI building blocks.[46, 47]

The degree of aggregation as a function of solvent composition is analysed using the equilibrium model developed by Korevaar and Meijer.[48, 49] It provides important insights into the thermodynamic parameters governing the assembly of the PDI building blocks. We exploited the 0-0/0-1 ratio as a function of DMF ratio in water to construct the "denaturation" curve for the representative **PDI-C$_3$Am-C$_2$OH** unit shown in Fig. 1B. The denaturation curves for the **PDI-C$_3$Am-C$_3$** and **PDI-C$_3$Im-C$_2$OH** units are shown in Fig. S1B and S2B, respectively. In the equilibrium model, the Gibb's free energy is made dependent on the DMF volume fraction following Eq. S3 where ΔG^0 represents the gain of Gibb's free energy upon monomer addition in pure water, and the m-value accounts for the change of ΔG as a function of DMF volume fraction (f). Please refer to Section 3 of the Supporting Information for a more detailed discussion. The thermodynamic parameters that regulate the assembly of **[PDI-C$_3$Am-C$_2$OH]$_{lfa}$**, **[PDI-C$_3$Am-C$_3$]$_{lfa}$**, and **[PDI-C$_3$Im-C$_2$]$_{lfa}$** assemblies are presented in Table 1. For the three studied PDI building blocks, the degree of cooperativity (sigma) is equal to one signalling that the growth of the respective aggregates is dictated by a monomer addition sharing an identical elongation constant, K_e, as represented in the inset of Fig. 1A. It is interesting to note that the elongation constant of the **PDI-C$_3$Im-C$_2$** building block is modestly lower than that calculated for the ammonium-derived **PDI-C$_3$Am-C$_2$OH**, and **PDI-C$_3$Am-C$_3$** units. This observation can be rationalized from the steric hindrance imposed by the imidazolium groups that can potentially destabilize the aggregation of the **PDI-C$_3$Im-C$_2$** building blocks when compared to the **PDI-C$_3$Am-C$_2$OH** and **PDI-C$_3$Am-C$_3$** analogues flanked with less sterically demanding ammonium side chains.

Concentration-dependent and variable-temperature studies are traditionally leveraged to probe the assembly mechanisms of supramolecular polymers. However, experimental challenges exist. To ensure the sampling of the entire aggregation process in variable-temperature studies, a solvated building block should exist as molecularly dissolved at high temperatures and under a fully aggregated state at low temperatures. The physical property of the solvent may impose a temperature window that hampers the accurate elucidation of a self-assembly mechanism. An appealing aspect of the equilibrium model developed by Korevaar and Meijer is the introduction of a correction factor p that accounts for an

Table 1. Thermodynamic Parameters Extracted from the Global Fitting of the Solvent-Dependent UV-vis Data

	PDI-C$_3$Am-C$_2$OH	PDI-C$_3$Am-C$_3$	PDI-C$_3$Im-C$_2$
σ	1	1	1
ΔG^0 (kJ mol^{-1})	-29	-28.75	-28
m (kJ mol^{-1})	16.5	17.15	14
K$_e$ (Mol^{-1})	1.4×10^5	1.3×10^5	10^5
DP at 200 μM	5.8	5.6	5
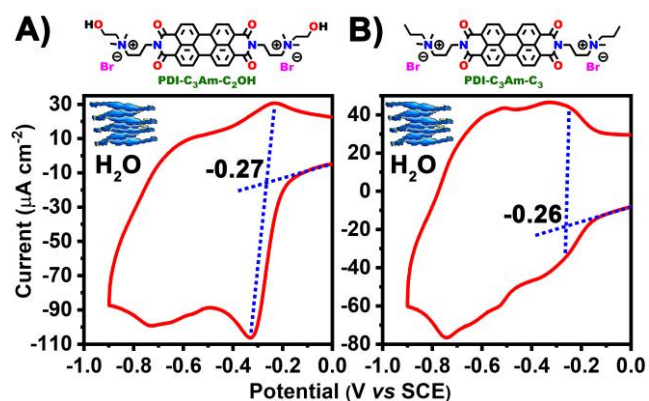
Fig. 2. Cyclic voltammograms recorded for the initially formed **assemblies [PDI-C₃Am-C₂OH]**_{Ifa} (A) and **[PDI-C₃Am-C₃]**_{Ifa} (B) in H₂O solvent under argon atmosphere. Experimental conditions: [analyte]=200 μM, 1 x PBS buffer, scan rate = 50 mV s-1, glassy carbon working electrode.

incomplete aggregate formation, or lack of saturation, under a given set of experimental conditions.

Fitting the denaturation curve of the three PDI building blocks required correction factors varying from 1.25 to 1.3 suggesting that these building blocks do not exist under a fully aggregated state in water at room temperature with a [PDI] ~ 20 μM. Please see Section 3 in the Supporting Information for more details. Fig. 1C illustrates this observation and chronicles the evolution of the concentration of PDI cores that are under an aggregated state ([**PDI**]$_{Aggregate}$) and molecularly dissolved ([**PDI**]$_{Monomer}$) as a function solvent composition for the representative **PDI-C₃Am-C₂OH** units. For a total concentration of PDI units C_{tot}= 20μM, a non-negligible population of the monomer exists as molecularly dissolved in pure water and suggests a non-complete polymerization process. The concentration distribution for the **PDI-C₃Am-C₃** and **PDI-C₃Im-C₂OH** units are shown in Fig. S1 and S2, respectively. Because ΔG^0 and m are independent of the total monomer concentration, the simulated curves showing the evolution of [PDI]$_{Aggregate}$ and [PDI]$_{Monomer}$ at C_{tot} = 200 μM are shown in Fig. 1C-(right panel). This concentration is representative of the building block concentration exploited during the redox-assisted process (*vide supra*) allowing us to confirm the aggregated states of the initial formed assemblies. As expected, a higher initial concentration of PDI building blocks leads to a drastic decrease of the total monomer population (less than 2%) that exists as molecularly dissolved at room temperature, in pure water. The **PDI-C₃Am-C₃** and **PDI-C₃Im-C₂** building blocks demonstrate identical concentration-dependent aggregation profiles as detailed in Section 3 of the Supporting Information. Further assessment of the degree of polymerization for the three assemblies indicates that an average of 5 to 6 repeating units comprise the aggregates at a concentration of 200 μM.[50]

Potentiometric Characterization of n-Doped PDI Supramolecular Polymers

The potentiometric properties elucidated for the [**PDI-C₃Am-C₂OH**]_{Ifa}, [**PDI-C₃Am-C₃**]_{Ifa}, and [**PDI-C₃Im-C₂**]_{Ifa} assemblies reveal that these π-conjugated supramolecular polymers evidence complex electronic structures in solution. Cyclic voltammetry (CV) experiments were performed on the three assemblies in 100% H₂O at C_{tot} = 200 μM, and the corresponding data are shown in Fig. 2 and S3. A common first reduction potential at ~ -0.27 V *vs* SCE is evidenced, and it indicates that these PDI-derived supramolecular polymers have some similarities in their electronic structure. While the [**PDI-C₃Am-C₂OH**]_{Ifa} assembly exhibits a distinct first reduction wave as shown in Fig. 2A, the [**PDI-C₃Am-C₃**]_{Ifa}, and [**PDI-C₃Im-C₂**]_{Ifa} assemblies are characterized by broad cathodic and anodic transitions that sample the 0 to -0.9-V electrochemical window. These observations suggest a non-negligible level of structural heterogeneity, in addition to a different solvation environment, that translates to electronic states that are distributed across a wide energy window. It is interesting to note that cyclic voltammograms recorded in a solvent mixture in which the assemblies exist primarily as molecularly dissolved (90% DMF- Fig. S4) show more resolved cathodic and anodic transitions reminiscent to these of individualized building blocks.[51] The chronicled potentiometric properties confirm that sacrificial electron donors characterized by an oxidation potential more negative than -0.30 V *vs* SCE are potential candidates to n-dope the PDI-derived supramolecular polymers in an aqueous solution.

The electronic spectral properties of the n-doped assemblies in an aqueous medium are examined and reveal the existence of π-anion stacks. Exploiting the inorganic (NaSH / Pathway 1- Scheme 1) and organic (DTT / Pathway 2/3-Scheme 1) sacrificial electron donors, reductive titrations of the initially formed assemblies **[PDI-C₃Am-C₂OH]**_{Ifa}, **[PDI-C₃Am-C₃]**_{Ifa}, and **[PDI-C₃Im-C₂]**_{Ifa} were conducted and the associated EAS are shown in Fig. 3A and S9-12. As shown in Fig. 3A, the addition of up to 0.3 eq. of NaSH to a solution of the **[PDI-C₃Am-C₂OH]**_{Ifa} assembly initiates the formation of reduced PDI aggregates as diagnosed by the emergence of the spectroscopic signatures centred at 990 nm, 816 nm, 733 nm, and 616 nm.[44, 52] A similar observation is made by gleaning the EAS of **[PDI-C₃Am-C₃]**_{Ifa} and **[PDI-C₃Im-C₂]**_{Ifa} n-doped with 0.3 eq NaSH (Fig. S9). Furthermore, it is important to note the apparition of a broad NIR band that covers the 1050-to-2500-nm spectral window that is initially centred at 1563 nm, 1576 nm, and 1565 nm for the **[PDI-C₃Am-C₂OH]**_{n-doped}, **[PDI-C₃Am-C₃]**_{n-doped}, and **[PDI-C₃Im-C₂]**_{n-doped} intermediates, respectively.

As shown in Fig. 3A and S9, the further addition of up to 1 eq. of NaSH is accompanied with profound modifications of the EAS sharing similar features among the three n-doped assemblies under investigation. For the exemplary **[PDI-C₃Am-C₃-C₂OH]**_{n-doped} assembly, while one of the spectroscopic fingerprints of an aggregated PDI anion centered at 991 nm vanishes as the equivalency of reductant is increased from 0.3 eq. to 1 eq., the loss of the resolved absorptive features observed in the visible to NIR spectral windows gives rise to a broad transition centered at 567 nm with two shoulders at 410

nm and 785 nm. The most striking observation is the evolution
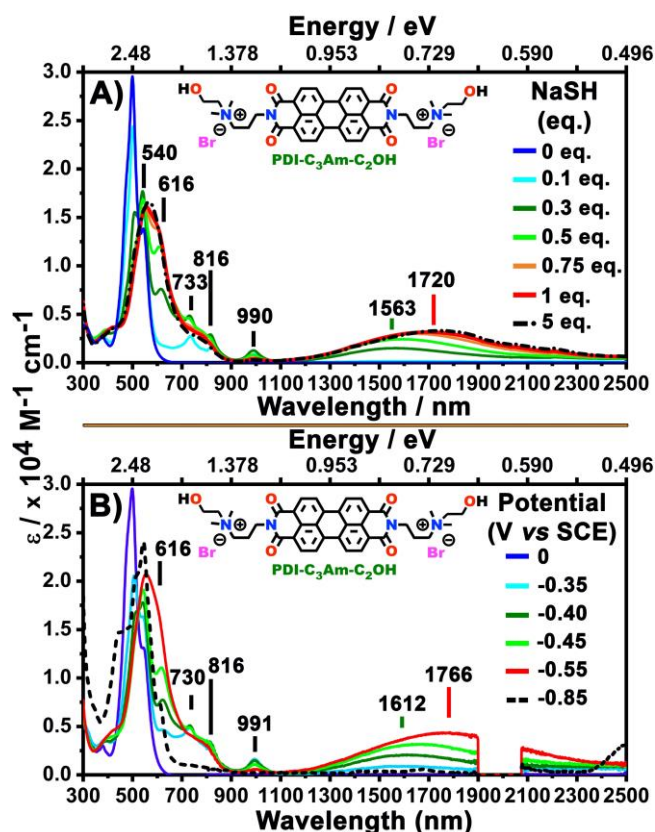
Fig. 3. UV-vis-NIR ground state electronic absorption spectra that narrate the: (A) reductive titration of the initially formed **[PDI-C₃Am-C₂OH]_lfa** assembly in deuterated water solvent exploiting sodium hydrosulfite (NaSH) as sacrificial electron donor, and (B) the electrochemically generated spectra in deuterated water. Experimental conditions: [PDI] = 200 μM (A and B); argon atmosphere; T = 20°C; optical pathlength = 2mm (A) and 1 mm (B); gold working electrode (B).

of the NIR transitions bathochromically shifted from 1563 nm to 1720 nm upon the addition of 1eq. of the sacrificial electron donor NaSH. Furthermore, while the spectral evolutions of **[PDI-C₃Am-C₃]_n-doped,** and **[PDI-C₃Im-C₂]_n-doped** intermediates share a similar trend to that underscored for **[PDI-C₃Am-C₂OH]_n-doped,** the n-doped **[PDI-C₃Im-C₂]_n-doped** assembly evidences a more modest bathochromic shift of the NIR band (51 meV) when compared to those established for **[PDI-C₃Am-C₂OH]_n-doped** (61 meV) and **[PDI-C₃Am-C₃]_n-doped** (66 meV). The spectra acquired upon the addition of up to 5 eq. of NaSH mimic those recorded after the addition of 1eq. of sacrificial electron donor, suggesting completion of the n-doping process.

Exploiting the organic reductant dithiothreitol (Pathway 2 – Scheme 1) does not alter the electronic properties of n-doped assemblies mimicking these observed when using NaSH as a sacrificial electron donor. As gleaned from the reductive titration and associated EAS chronicled in Fig. S10-12, similar spectral evolutions to those evidenced when using NaSH as a sacrificial electron donor are witnessed upon n-doping the initially formed **[PDI-C₃Am-C₂OH]_lfa, [PDI-C₃Am-C₃]_lfa** and **[PDI-C₃Im-C₂]_lfa** assemblies. Spectroscopic signatures that indicate

the formation of aggregated radical PDI states are followed by the emergence of absorptive features in the 400-to-900-nm spectral window concomitant with the redshift of the broad NIR transitions. All taken together, the NaSH and DTT reductive titrations suggest the emergence of similar electronic states in the n-doped **[PDI-C₃Am-C₂OH]_n-doped, [PDI-C₃Am-C₃]_n-doped** and **[PDI-C₃Im-C₂]_n-doped** intermediates that diagnose a substantial degree of PDI-PDI interaction. To confirm that the NIR absorptive features are intrinsic spectroscopy properties of the n-doped aggregates, an exemplary reductive titration utilizing a molecular surfactant was conducted on the **[PDI-C₃Am-C₂OH]_lfa** assembly and is presented in Fig. S14. Following the formation of the n-doped intermediate, the addition of 100 eq. of the molecular surfactant sodium dodecyl sulfate (SDS) triggers the formation of individualized PDI radical anions as indicated by the recovery of the well-resolved spectroscopic signatures located at 962, 720, and 602 nm.

To gain more insights into the electrochemical potentials associated with the spectroscopic signatures of the n-doped intermediates, electrochemically generated spectra of the **[PDI-C₃Am-C₂OH]_n-doped, [PDI-C₃Am-C₃]_n-doped** and **[PDI-C₃Im-C₂]_n-doped** intermediates are acquired and are shown in Fig. 3B and Fig. S5-S7, respectively. For the three assemblies, the spectroscopic profiles of the n-doped intermediates, generated with 1 and 5 eq. of chemical reductant (NaSH or DTT), are perfectly reproduced at a potential of -0.55 V *vs* SCE. The apparent redshifts of the NIR transitions when comparing the electrochemically (1766 nm) with the chemically (1720 nm) induced spectra may originate from the nature of the cations paired with the nascent negative charges. It is interesting to note that the spectrum recorded at a potential of -0.60 V *vs* SCE mimics that monitored at -0.55 V, suggesting the saturation of the n-doped intermediates with electrons. Incrementing the potentials to -0.65 V is accompanied with the decrease of the NIR transitions in addition to the apparition of new spectroscopic features centered at 540 nm and 448 nm. Further excursion towards more cathodic potentials (-0.85 V *vs* SCE) reinforce the absorptive signatures characteristic of the PDI dianion species (Fig. S5-S7).

The reductive titration experiments combined with the UV-vis-NIR spectroelectrochemistry experiments deliver preliminary conclusions on the origin of the NIR transitions
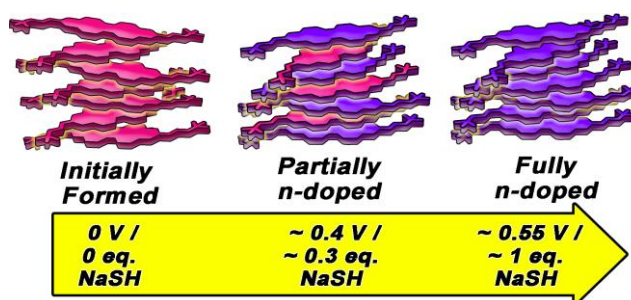
Scheme 2. Representation of the level of n-doping of an initially formed assembly as a function of applied cathodic potential and concentration of sacrificial electron acceptor.
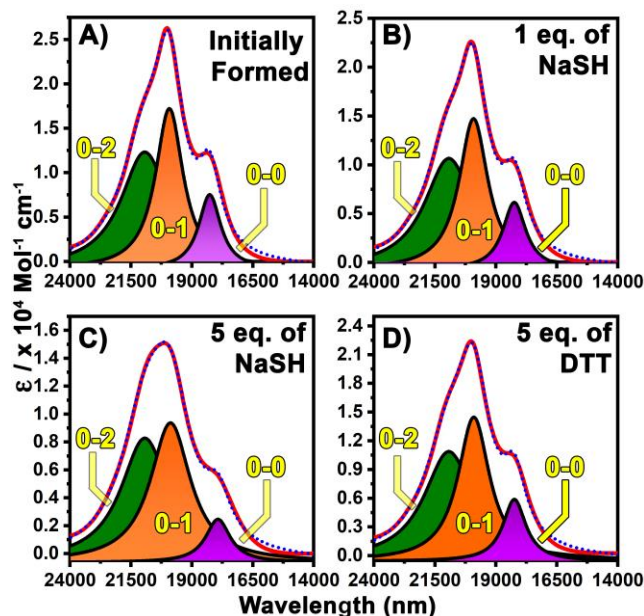
Fig. 4. Representative electronic absorption spectra recorded for the initially formed **[PDI-C₃Am-C₂OH]Cont** assembly (A), and the neutral, redox-treated **[PDI-C₃Am-C₂OH]Rta** assemblies generated after oxidizing the n-doped intermediates initially formed with 1eq. of NaSH (B), 5eq. of NaSH (C), and 5 eq. of DTT (D). The area under curve in purple, orange and green have been calculated using a nonlinear regression fitting (Lorentzian) and correspond to the 0-0, 0-1, and 0-2 vibronic transition, respectively. The reconstructed absorption spectra from the fit are shown in dotted blue line.

characterizing the n-doped intermediates. As suggested by the electrochemically generated spectra, a first n-doped state is formed up to a potential of -0.40 V and is represented schematically in Scheme 2. A similar state is accessed when using a low equivalency of sacrificial electron donor (~ 0.3 eq. vs PDI units). For the exemplary **PDI-C₃Am-C₂OH** building block, the corresponding n-doped intermediate is characterized by the transitions centered at 1612 nm, 991 nm, 816 nm, 730 nm and 616 nm. It is fair to assume that increasing the potential to -0.55 V enables the formation of highly doped intermediates at the origin of the NIR transition lying lower in energy when compared to that of the species formed at -0.35 V. A similar pattern is observed in the reductive titration experiments. Furthermore, an increase of only 0.05 V towards cathodic potentials (- 0.60 V to -0.65 V) initiates the formation of PDI dianions which become the major reduced species at -0.85 V. All taken together, this data suggests that the negatively charged intermediates formed at -0.55 V can be described as heavily n-doped where most of the PDI units comprising the aggregates exist under a reduced state.

We postulate that the NIR transition observed at -0.55 V originates from novel electronic states formed by interaction of the PDI radical anions in the n-doped SPs. In this regard, it is interesting to note that n-doped **[PDI-C₃Im-C₂]n-doped** intermediates feature the highest NIR transition energy among the three PDI systems under investigation. Concomitantly, the

PDI-C₃Im-C₂ building block evidences the lowest elongation constant at room temperature. Less likely to be coincidental, these observations may originate from the steric hindrance imposed by the imidazolium side chains that decrease the degree of interchromophore interaction both in the neutral and in the n-doped state. Seminal work by Miller has reported closely related phenomena for n-doped water-soluble naphtalene diimides derivatives.[53-55]

Tuning the Excitonic Properties

Because weak, non-covalent interactions regulate the conformation of supramolecular constructs, stacks of π-conjugated cores are fragile matter compositions where minor perturbations of the interchromophore geometry can perturb the excitonic properties at the assembly level. Pioneering studies by Spano have unambiguously demonstrated that Angstrom-level displacement engenders a drastic modification of the excitonic coupling in PDI-based H-like aggregates.[24, 56, 57] To glean further insights into the extent to which the n-doping of π-stacks can be exploited to tune the electronic properties of non-covalent assemblies, the model developed by Spano for H-like aggregates was exploited to calculate and compare the Ex_{BW} of the initially formed assemblies **[PDI-C₃Am-C₂OH]Ifa**, **[PDI-C₃Am-C₃]Ifa**, and **[PDI-C₃Im-C₂]Ifa** to those of the final, redox-treated superstructures formed by aerating the n-doped intermediates over 48 hours. Because excitonic properties in non-covalent assemblies are intimately related to interchromophore interaction and building block conformations, elucidating the Ex_{BW} for each of the pathways shown in Scheme 1 provides a means to evaluate potential structural reconfigurations throughout the redox-assisted assembly pathways.

The electronic spectral properties of the redox-treated PDI assemblies **[PDI-C₃Am-C₂OH]**, **[PDI-C₃Am-C₃]**, and **[PDI-C₃Im-C₂]** differ as a function of the chemical reductants (Pathway 1-3, Scheme 1). Fig. 4 chronicles the representative EAS for the initially formed [**PDI-C₃Am-C₂OH**] assembly and the related redox-treated superstructures formed after oxidizing the n-doped state. Please note that 48 hours separates the data

Table 2. Calculated Free Exciton Bandwidth (Ex_{BW}) in meV for the Three Assemblies as a Function of the n-Doping Conditions Used in the Redox-Assisted Assembly Pathway 1-2.

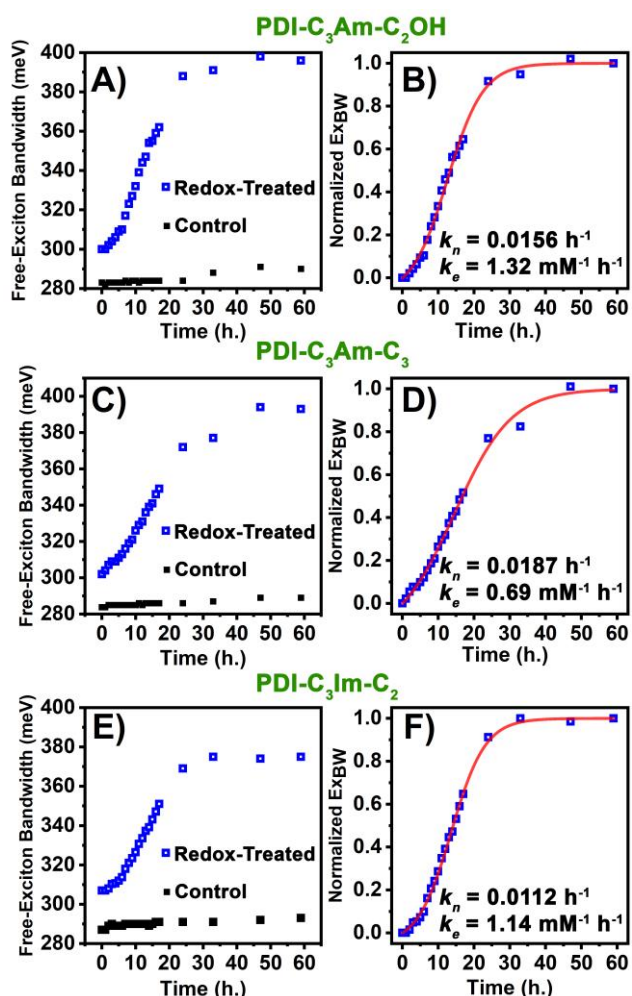|	PDI-C₃Am-C₂OH	PDI-C₃Am-C₃	PDI-C₃Im-C₂
Initially Formed	280	281	283
Control	290	290	292
DTT (5 eq.)	323	310	325
NaSH (1eq.)	310	309	303
NaSH (5eq.)	395	395	375
DTT/Na₂SO₃	396	n/a	n/a

Fig. 5. (A,C,E) Evolution of the free-exciton bandwidth as a function of time for the control assemblies and the redox-treated superstructures formed with 5eq. of NaSH. (B,D,F) Normalized Ex_{BW} as a function of time calculated for the redox-treated assemblies. The experimental data (open blue square) is fitted using the nucleation-growth 2-step model introduced by Finke and Watsky. Please refer to Section 6 of the Supporting Information for more details.

collection from the oxidation of the reduced intermediates. While the EAS recorded for the redox-treated superstructures formed with 1eq. of NaSH and 5eq. of DTT evidence spectroscopic features similar to those that characterize the initially formed assembly, non-negligible perturbations of the absorptive properties are diagnosed for the superstructure engendered using 5eq. of NaSH. A pronounced redistribution of the oscillator strength of the 0-0 vibronic transition into the 0-1 and 0-2 vibronic transition is evidenced, in addition to a ~300 cm^{-1} hypsochromic shift of the 0-0 transition. Congruent with these spectroscopic features, an increase of more than 33% of the Ex_{BW} is evidenced in the redox-treated superstructure ^{NaSH}[PDI-C$_3$Am-C$_2$OH]$_{Rts}$ formed through Pathway 1. Table 2 summarizes the calculated Ex_{Bw} as a function of n-dopant equivalency and chemical properties. To rule out that the reported increase of Ex_{Bw} originates solely form the interaction of salts produced during the oxidation of the excess of NaSH

reductant, the Ex_{BW} of the control samples was investigated. Theses control samples were generated by adding an aerated solution comprising oxidized NaSH (5 eq.) to a solution of the initially formed assembly **[PDI-C$_3$Am-C$_2$OH]$_{Ifa}$**. As can be seen in Fig. S15 and Table 2, no noticeable perturbation of the EAS is witnessed, and the calculated Ex_{BW} for the controlled assembly **[PDI-C$_3$Am-C$_2$OH]$_{Cont}$** remains virtually unperturbed (< 4%) when compared to that of the pristine **[PDI-C$_3$Am-C$_2$OH]$_{Ifa}$** assembly.

The redox-treated superstructures **[PDI-C$_3$Am-C$_3$]$_{Rts}$**, and **[PDI-C$_3$Im-C$_2$]$_{Rts}$** formed through Pathway 1 exhibit similar electronic spectral properties to those elucidated for the analog **PDI-C$_3$Am-C$_2$OH** building blocks, as shown in Fig. S16 and S17. As gleaned in Table 2, a non-negligible increase of Ex_{BW} is observed for assemblies n-doped with 5eq. of NaSH while only a modest evolution of the Ex_{BW} is notable when 1eq. of NaSH and 5eq. of DTT are exploited. Furthermore, it is important to note that, as confirmed by the control experiment, the sole products generated from the oxidation of NaSH are not responsible for the increase of Ex_{BW}. All taken together, the data presented thus far indicate that: 1) the imidazolium side chains flanked on the PDI cores engender superstructures equipped with a lower Ex_{BW} when compared to superstructures that feature ammonium groups, 2) the formation of n-doped intermediates is critical to increase the Ex_{BW}, and 3) additional parameters have to be accounted for to rationalize the increase of Ex_{BW} exclusively evidenced in the reaction Pathway 1 that exploits 5eq. of NaSH.

As shown in Fig. 5, which chronicles the evolution of the Ex_{BW} , as a function of time recorded for the ^{NaSH}**[PDI-C$_3$Am-C$_2$OH]$_{Rts}$,** ^{NaSH}**[PDI-C$_3$Am-C$_3$]$_{Rts}$,** and ^{NaSH}**[PDI-C$_3$Im-C$_2$]$_{Rts}$** superstructures, the Ex_{BW} measured for assemblies that are n-doped using 5 eq. of NaSH (Pathway 1 − Scheme 1) increases over the 48 hours following redox treatment. The three assemblies share a similar trend: the modest increase of Ex_{BW} (< 7%) witnessed within the first 8 hours after neutralizing the n-doped intermediates is followed by a drastic augmentation between 8 to 40 hours that plateaus afterwards. In sharp contrast, the control samples do not evidence a meaningful evolution of the recorded Ex_{BW}, but instead, fluctuates in the 280-to-290-meV energy range. Because the functions of non-covalent assemblies are defined by their structure, the dynamic increase of Ex_{BW} suggests that the conformation of the redox-treated superstructures, created immediately after oxidation, evolves as a function time.

A nucleation-growth mechanism, exclusive to Pathway 1, governs the aggregation of the redox-treated ^{NaSH}**[PDI-C$_3$Am-C$_2$OH]$_{Rts}$,** ^{NaSH}**[PDI-C$_3$Am-C$_3$]$_{Rts}$,** and ^{NaSH}**[PDI-C$_3$Im-C$_2$]$_{Rts}$** superstructures. The sigmoidal shape that characterizes the increase of Ex_{BW} as a function of time, shown in Fig. 5, is reminiscent to kinetic data reported for protein aggregation. More specifically, the general 2-step kinetic model introduced by Finke and Watzky (F-W) has been widely applied to fit protein aggregation and features a nucleation step followed by an autocatalytic growth step.[58-61] This model is exploited to

successfully fit ($R^2 > 0.99$) the normalized increase of Ex_{BW} as a function of time in Fig. 5. For the three assemblies, a similar nucleation rate constant bracketed between 0.01 and 0.02 h^{-1} (k_n) is evidenced where the elongation rate constant (k_e) varies from 0.69 mM^{-1} h^{-1} for the [**PDI-C$_3$Am-C$_3$**]$_{Rts}$ superstructure to 1.32 mM^{-1} h^{-1} for the [**PDI-C$_3$Am-C$_2$OH**]$_{Rts}$ superstructure. While we acknowledge that the 2-step F-W mechanism is a simplified model that condenses and averages a plethora of steps into two pseudo-elementary steps, it provides valuable insights into the possible mechanisms that regulates the growth of the redox-treated superstructures. It is important to note that perturbation of the structure-function properties of neutral, water-soluble PDI assemblies upon redox treatment has also been reported by Hermans and further bolsters our analysis.[42]

To rationalize the data presented thus far, we postulate that Pathway 1 in Scheme 1B enables the creation of metastable architectures initiated immediately after the oxidation step; their further nucleation and growth engender superstructures with increased Ex_{BW}. It is interesting to note that at t = 0 h, the redox-treated assemblies are characterized by an Ex_{BW} modestly larger than that recorded for the control samples. This change in excitonic properties further confirms the formation of supramolecular constructs that differ from the initially formed assemblies. In addition, the fact that 5eq. of NaSH is necessary to record a substantial change in the excitonic properties indicates that the oxidized NaSH products are necessary to promote the growth of the final superstructures. While the oxidation of NaSH can generate several byproducts, sodium hydrosulfite Na$_2$SO$_3$ salt is one of the predominant species. We hypothesized that this byproduct may participate in the growth of the superstructures.

Reductive titration experiments that combine the sacrificial electron donor DTT and the addition of sodium sulfite (Na$_2$SO$_3$) provide insights into parameters that regulate the increase of Ex_{BW} in PDI assemblies solvated in an aqueous medium. Because n-doping the initially formed PDI assemblies with the organic reductant DTT does not enforce the same increase of Ex_{BW} elucidated in Pathway 1, we leveraged this condition to unveil the potential role played by the sulfite anion in the redox-assisted assembly process. To test our hypothesis, we exploited the [**PDI-C$_3$Am-C$_2$OH**] building blocks as an exemplary platform. In this experiment, the [**PDI-C$_3$Am-C$_2$OH**]$_{n-doped}$ intermediate was generated by the addition of 5 eq. of DTT and 5 eq. of Na$_2$SO$_3$ (Pathway 3 in Scheme 1B). The associated EAS are chronicled in Fig. S13 and demonstrate identical spectroscopic signatures to these recorded for the n-doped assemblies formed using 5eq. of NaSH. This observation suggests that these two pathways, namely DTT/Na$_2$SO$_3$ and NaSH-5eq., generate n-doped intermediates equipped with similar electronic structures.

The EAS and Ex_{BW} presented in Fig. S18 underscore the non-negligible role played by the sulfite anion in regulating the electronic spectral properties of the redox-treated superstructures [**PDI-C$_3$Am-C$_2$OH**]$_{Rts}$. As gleaned in Fig. S18C, the reductive titration of the [**PDI-C$_3$Am-C$_2$OH**]$_{Ifa}$ assembly with

DTT/Na$_2$SO$_3$ leads to the formation of the redox-treated assembly $^{DTT/Na_2SO_3}$[**PDI-C$_3$Am-C$_2$OH**]$_{Rts}$ that evidences an Ex_{BW} (396 meV) after 48 hours, similar to that observed in the titration that exploits 5eq. of NaSH (Pathway 1). Please note that control samples for Pathway 3 are shown in Fig. S18A-B and do not suggest that the increases of Ex_{BW} stems solely from Na$_2$SO$_3$. The kinetic data shown in Fig. S19 chronicles the change of Ex_{BW} as a function of time for the $^{DTT/Na_2SO_3}$[**PDI-C$_3$Am-C$_2$OH**]$_{Rts}$ assembly formed exploiting Pathway 3 (Scheme 1B) and reveals that an alternative aggregation process, rather than a nucleation-growth mechanism, dictates the formation of these supramolecular architectures. Please refer to the Section 7 of the Supporting Information for a more detailed discussion. From these preliminary kinetic analyses, it is fair to infer that the chemical composition of the salts produced during the redox treatment process plays an important role in assisting the reconfiguration of the parent assemblies. In all likelihood, the oxidation of the excess of NaSH reductant engenders the formation of a more complex salt mixture involved in the growth of the final redox-treated superstructures. Analysis of the solid-state morphologies confirms this hypothesis.

Solid-State Morphologies

Interrogating the solid-state morphologies of the redox-treated ^{NaSH}[**PDI-C$_3$Am-C$_2$OH**]$_{Rts}$, ^{NaSH}[**PDI-C$_3$Am-C$_3$**]$_{Rts}$, and
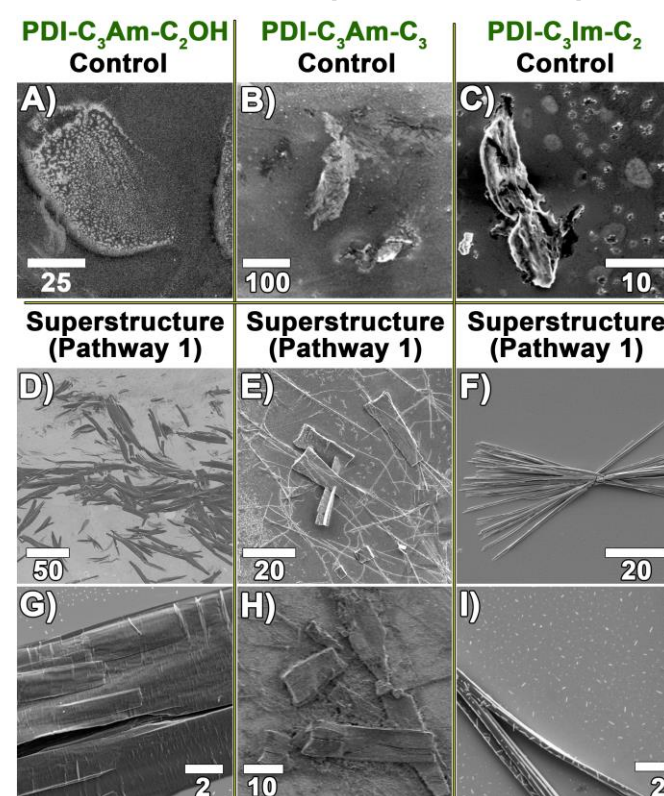
Fig. 6. SEM images recorded for the control assemblies [**PDI-C$_3$Am-C$_2$OH**]$_{Cont}$ (A), [**PDI-C$_3$Am-C$_3$**]$_{Cont}$ (B), and [**PDI-C$_3$Im-C$_2$**]$_{Cont}$ (C). Hierarchical solid-materials that characterize the redox-treated superstructures [**PDI-C$_3$Am-C$_2$OH**]$_{Rts}$ (D,G), [**PDI-C$_3$Am-C$_3$**]$_{Rts}$ (E,H), and [**PDI-C$_2$Im-C$_2$**]$_{Rts}$ (F,I). These SEM images correspond to the solid-state morphologies formed by dropcasting the parent, water solution on a silicon wafer. Scale bars = μm.
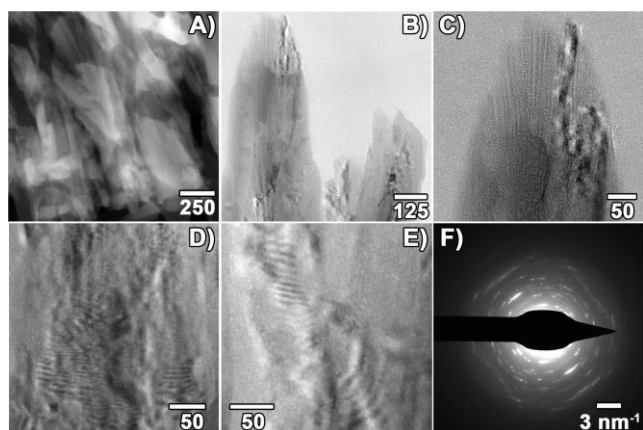
Fig. 7. TEM images of the redox-treated superstructure [**PDI-C₃Am-C₂OH**]$_{Rts}$ (A-E). The rod-like nanostructures observed in panel D and E are characterized by a width of 3 nm and correspond to the elementary π-conjugated supramolecular polymer (π-stack) comprising the assemblies shown in (A-C). (F) Selected area electron diffraction acquired on the hierarchical superstructures shown on A. Scale bar units = nm.

^{NaSH}[**PDI-C₃Im-C₂**]$_{Rts}$ superstructures reveals the formation of hierarchical mesoscale objects exclusively detected in the redox-assisted assembly Pathway 1 that exploits 5 eq. of NaSH. Fig. 6 chronicles the SEM images recorded for the three redox-treated superstructures after dropcasting the parent aqueous solutions on a silicon-oxide-coated substrate. While the ^{NaSH}[**PDI-C₃Am-C₂OH**]$_{Rts}$ and ^{NaSH}[**PDI-C₃Am-C₃**]$_{Rts}$ superstructures initiate the creation of ribbon-like materials which can span more than 65 μm in length with an associated width of 14 μm, as shown in Fig. 6D,6G, 6E, and 6H, the ^{NaSH}[**PDI-C₃Im-C₂**]$_{Rts}$ superstructure evolves toward high-aspect ratio fiber-like materials. To validate reproducibility, additional SEM images are shown in Fig. S20. The fact that both ^{NaSH}[**PDI-C₃Am-C₂OH**]$_{Rts}$ and ^{NaSH}[**PDI-C₃Am-C₃**]$_{Rts}$ superstructures enable the formation of seemingly 2D objects whereas the ^{NaSH}[**PDI-C₃Im-C₂**]$_{Rts}$ superstructure evolves into 1D microstructures, highlights the non-innocent role played by the cationic side chains in dictating the solid-state morphologies of the superstructures. Because the mesoscale objects shown in Fig. 6 derived from lateral interactions between π-stacks, we postulate that the imidazolium side chains hamper the growth of the ribbon-like materials exclusively engendered when the PDI cores are flanked with small ammonium cationic groups.

In sharp contrast, the SEM images chronicled in Fig. S22-S23 indicate that assemblies treated with 1eq. of NaSH and 5eq. of DTT lack the ability to form hierarchical solid-state materials, as do the control assemblies shown in Fig. 6 and S21. Similarly, the $^{DTT/Na_2SO_3}$[**PDI-C₃Am-C₂OH**]$_{Rts}$ assemblies formed using Pathway 3 (DTT/Na₂SO₃) do not initiate the formation of organized solid-state constructs as shown in Fig. S24 and S25. All taken together, these findings indicate that: 1) the formation of hierarchical materials is exclusive to superstructures formed via a nucleation-growth mechanism (Pathway 1 - Scheme 1), and 2) the drastic change of solid-state morphologies signals a

reconfiguration of the initially formed assemblies only observed when Pathway 1 in the redox-assisted assembly process is taken.

To glean more insights into the solid-sate morphologies at the nanoscale dimension, TEM images are recorded for the representative ^{NaSH}[**PDI-C₃Am-C₂OH**]$_{Rts}$ superstructures and are shown in Fig. 7. Characterized by fiber-like materials, the images in Fig. 7 suggest that the ribbon-shaped materials observed by SEM in Fig. 6D and 6G are composed by interacting 1-dimensional subcomponents. Furthermore, elementary fibers can be detected on the zoom-in region in Fig. 7B and 7C and demonstrate a width varying from 15 to 21 nm. Local crystalline domains with substantially ordered phases within the fibrous nanostructures are detected by electron diffraction, as shown in Fig. 7F. Further corroboration of this fact emerges from the presence of well-resolved periodic lattice fringes, known as 'moiré fringes', with the periodic distance of ~3 nm in the nanostructures shown in Fig.s 7D and 7E.[62-66] This observation confirms the presence of local crystalline domains, and consequently periodicity in the long-range ordering of the 1D π-conjugated supramolecular polymeric chains that are constituents of the overall hierarchical fiber-like superstructures. The rod-like morphologies easily discerned in Fig. 7D and 7E are characterized by a width of ~ 3 nm that matches the size of one **PDI-C₃Am-C₂OH** building block as indicated by the energy-minimized structure performed at the DFT level of theory (Section 9 of the Supporting Information). This relationship indicates that the observed nanoscale objects correspond to elementary stacks of π-conjugated building blocks.

Structure-Function Relationships

Correlating the reductive titration experiments with the change of excitonic properties, and the solid-state morphologies evidenced by the redox-treated superstructures formed during Pathway 1, delivers important consideration to modulate the structure-function relationships of redox active supramolecular polymers. Not only is the formation of n-doped intermediates a required step, but the nucleation-growth step of the redox-treated assemblies appears equally important to access superstructures that demonstrate an increase of Ex_{BW} and are capable of forming hierarchical materials.

It is fair to consider that a structural reorganization of the π-conjugated supramolecular polymers accompanies the injection of negative charge carriers. Preliminary DFT calculations performed on a model aggregate built from three truncated PDI repeating units supports this hypothesis. Fig. 8A compares the electrostatic potential map of an energy minimized PDI trimer structure under a neutral state ([PDI]₃), and in a n-doped state ([PDI]₃³⁻). As can be gleaned for [PDI]₃, a slipped geometry best describes the conformation of this representative neutral trimer where: 1) a distance of 3.45 Å separates the PDI planes, and 2) a twist angle of 23.4° defines the rotational offset between the repeating units. Electrostatic interactions between the carbonyl groups of the imide
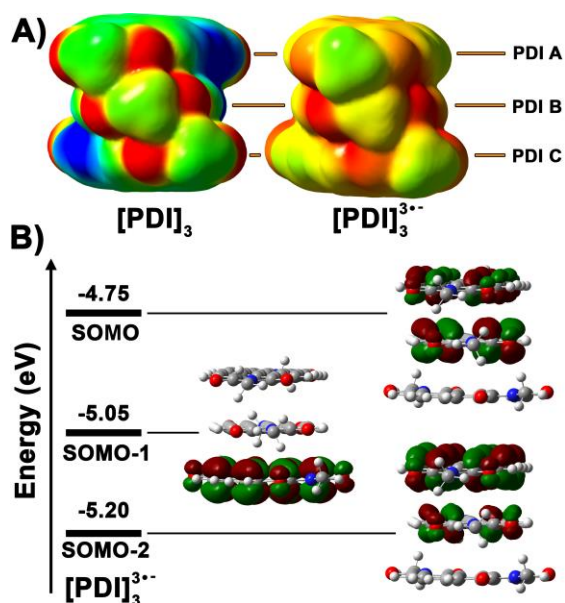
Fig. 8. (A) Energy-minimized structures of a representative π-conjugated supramolecular polymer that feature three PDI repeating units. The neutral $[PDI]_3$ and fully n-doped $[PDI]_3^{3-}$ are represented. Please note that a truncated PDI unit where the side chains have been replaced by a methyl group is used. (B) Frontier orbital diagram for $[PDI]_3^{3-}$. Computational method: DFT = ωB97X-D, basis set = cc-pvdz, solvent =water.

functions and the methyl side chains may be a major contributor to the apparent slipped geometry. As shown in Fig. 8A, the energy-minimized structure calculated for the n-doped PDI trimer $[PDI]_3^{3-}$ underscores a non-negligible degree of structural reorganization. More specially, the conformation of PDI A and PDI B is characterized by a twist angle of 13.2° that contrasts the 23.4° angle delineated by the parent, neutral trimer. It is also interesting to note that while a distance of 3.4 Å separates PDI A and PDI B, PDI B and PDI C are separated by 3.6 Å. This increase of interplanar distance may underscore the existence of electrostatic repulsion between PDI radical anions comprising this model aggregate.

To glean more insights into the electronic structure of the model n-doped aggregate, Fig. 8B chronicles the frontier molecular orbitals computed for $[PDI]_3^{3-}$. Notably, the wavefunctions characterizing the SOMO and the SOMO-2 are delocalized over the PDI A and B repeating units. This observation may diagnose a non-negligible degree of interaction between the PDI radicals comprising the n-doped trimer model that may be at the origin of the broad NIR transitions observed for the n-doped intermediates. While we acknowledge that the DFT calculation performed on the trimer model aggregate oversimplifies the structure-function complexity of the n-doped intermediates reported in this study, we suggest that it provides further evidences that structural reorganization accompanies electron injections into the conduction band of neutral PDI-derived supramolecular polymers.

The species formed following oxidation of the n-doped intermediates are likely to bear some of the conformational

modifications dictated by the reduced π-conjugated SPs. Note that the slight increase of Ex_{BW} evidences from all the reductive titration experiments support this claim. Furthermore, the increase of Ex_{BW} as a function of time for the reductive titration that exploits 5eq. of NaSH reveals that the products formed by oxidation of the excess of NaSH further assist the growth of the reconfigured superstructures. The dynamic increase of Ex_{BW} diagnoses a non-negligible change of superstructure conformation that is further confirmed by the formation of hierarchical mesoscale materials in the solid-state.

While evidencing an increase of Ex_{BW} comparable to that of the reconfigured $^{NaSH}[PDI-C_3Am-C_2OH]_{Rts}$ superstructure formed through Pathway 1, the redox treated $[PDI-C_3Am-C_2OH]_{Rta}$ assembly generated with DTT/Na_2SO_3 (Pathway 3 – Scheme 1) takes an alternative aggregation route. This assumption is supported by the kinetic analysis tracing the increase of Ex_{BW} as a function of time and the corresponding solid-state morphologies. The redox-assisted assembly pathway 3 does not engender the formation of hierarchical mesoscale materials comparable to those delineated by the reconfigured superstructure $^{NaSH}[PDI-C_3Am-C_2OH]_{Rts}$. This observation indicates that the nucleation-elongation mechanism, exclusively monitored for the assemblies treated with 5 eq. of NaSH, is a required step to access organized solid-state materials. While a matter of speculation at this time, we hypothesize that the conformation of the reconfigured superstructures in solution (Pathway 1 – Scheme 1) may, to some extent, differs from that of the redox-treated assembly (pathway 3 – Scheme 1) consequently leading to different packing configurations formed during the dropcasting process.

Conclusions

In conclusion, we provide the first, general understanding of the parameters required to modulate the excitonic properties of π-conjugated supramolecular polymers through redox-assisted assembly. The properties of the initially formed assemblies are characterized using a solvent-dependent equilibrium model and reveals that an average of 5 to 6 PDI building blocks comprise the H-like aggregates. The electrochemical and chemical reduction of these non-covalent assemblies enable the formation of n-doped π-stacks that present significant degree of electron-electron interaction as indicated by the rise of novel spectroscopic transitions in the NIR spectral window. Oxidation of the n-doped intermediates produces redox-treated assemblies which Ex_{BW} increases as a function of time. Kinetic data analysis reveals that a nucleation-elongation mechanism governs the growth of assemblies formed immediately after neutralization of the n-doped stacks. This finding indicates that electron injection into the conduction bands of the PDI-derived supramolecular polymers open a new pathway in the aggregation energy landscape and yield superstructure demonstrating non-negligible level of structural reconfiguration.

Interrogation of the solid-state morphologies recorded for the redox-treated assemblies using HRTEM and SEM unveils the

formation of hierarchical mesoscale materials that are exclusively evidenced for the superstructures formed by a nucleation-growth mechanism. We elucidate that the modulation of the structure-function relationships evidenced by the PDI-derived assemblies is intimately corelated to the sacrificial electron donor properties and underscores a synergistic effect between the products formed during the redox-assisted assembly process. Not only does this study deliver a general tool to regulate the excitonic properties of PDI-based aggregates, but it also refines the rules and principles to orchestrate the creation of hierarchical organic matter compositions. In addition, increasing excitonic coupling of organic assemblies paves the way to engineer materials composition relevant to solar energy capture, conversion, and storage.[8, 10, 67-69]

Conflicts of interest

There are no conflicts to declare.

Acknowledgements

Notes and references

1. Wasielewski, M. R., *Acc. Chem. Res.* **2009,** *42*, 1910-1921.
2. Mativetsky, J. M.; Orgiu, E.; Lieberwirth, I.; Pisula, W.; Samorì, P., *Adv. Mater.* **2014,** *26*, 430-435.
3. Caram, J. R.; Doria, S.; Eisele, D. M.; Freyria, F. S.; Sinclair, T. S.; Rebentrost, P.; Lloyd, S.; Bawendi, M. G., *Nano Lett.* **2016,** *16*, 6808-6815.
4. Liang, N.; Sun, K.; Zheng, Z.; Yao, H.; Gao, G.; Meng, X.; Wang, Z.; Ma, W.; Hou, J., *Adv. Energy Mater.* **2016,** *6*, 1600060.
5. Di Nuzzo, D.; Kulkarni, C.; Zhao, B.; Smolinsky, E.; Tassinari, F.; Meskers, S. C. J.; Naaman, R.; Meijer, E. W.; Friend, R. H., *ACS Nano* **2017,** *11*, 12713-12722.
6. Bullard, G.; Tassinari, F.; Ko, C.-H.; Mondal, A. K.; Wang, R.; Mishra, S.; Naaman, R.; Therien, M. J., *J. Am. Chem. Soc.* **2019,** *141*, 14707-14711.
7. Olivier, J.-H.; Park, J.; Deria, P.; Rawson, J.; Bai, Y.; Kumbhar Amar, S.; Therien Michael, J., *Angew. Chem. Int. Ed.* **2015,** *54*, 8133-8138.
8. Sung, J.; Nowak-Król, A.; Schlosser, F.; Fimmel, B.; Kim, W.; Kim, D.; Würthner, F., *J. Am. Chem. Soc.* **2016,** *138*, 9029-9032.
9. Kulkarni, C.; Mondal, A. K.; Das, T. K.; Grinbom, G.; Tassinari, F.; Mabesoone, M. F. J.; Meijer, E. W.; Naaman, R., *Adv. Mater.* **2020,** *32*, 1904965.

10. Sung, J.; Kim, P.; Fimmel, B.; Würthner, F.; Kim, D., *Nat. Commun.* **2015,** *6*, 8646.
11. Le, A. K.; Bender, J. A.; Roberts, S. T., *J. Phys. Chem. Lett.* **2016,** *7*, 4922-4928.
12. Le, A. K.; Bender, J. A.; Arias, D. H.; Cotton, D. E.; Johnson, J. C.; Roberts, S. T., *J. Am. Chem. Soc.* **2018,** *140*, 814-826.
13. Haedler, A. T.; Kreger, K.; Issac, A.; Wittmann, B.; Kivala, M.; Hammer, N.; Köhler, J.; Schmidt, H.-W.; Hildner, R., *Nature* **2015,** *523*, 196-199.
14. Coropceanu, V.; Cornil, J.; da Silva Filho, D. A.; Olivier, Y.; Silbey, R.; Brédas, J.-L., *Chem. Rev.* **2007,** *107*, 926-952.
15. Mas-Torrent, M.; Rovira, C., *Chem. Rev.* **2011,** *111*, 4833-4856.
16. Ostroverkhova, O., *Chem. Rev.* **2016,** *116*, 13279-13412.
17. Gélinas, S.; Rao, A.; Kumar, A.; Smith, S. L.; Chin, A. W.; Clark, J.; van der Poll, T. S.; Bazan, G. C.; Friend, R. H., *Science* **2014,** *343*, 512.
18. Bakulin, A. A.; Rao, A.; Pavelyev, V. G.; van Loosdrecht, P. H. M.; Pshenichnikov, M. S.; Niedzialek, D.; Cornil, J.; Beljonne, D.; Friend, R. H., *Science* **2012,** *335*, 1340.
19. Chen, X.-K.; Ravva, M. K.; Li, H.; Ryno, S. M.; Brédas, J.-L., *Adv. Energy Mater.* **2016,** *6*, 1601325.
20. Heitzer, H. M.; Savoie, B. M.; Marks, T. J.; Ratner, M. A., *Angew. Chem. Int. Ed.* **2014,** *53*, 7456-7460.
21. Jackson, N. E.; Kohlstedt, K. L.; Savoie, B. M.; Olvera de la Cruz, M.; Schatz, G. C.; Chen, L. X.; Ratner, M. A., *J. Am. Chem. Soc.* **2015,** *137*, 6254-6262.
22. Vura-Weis, J.; Ratner, M. A.; Wasielewski, M. R., *J. Am. Chem. Soc.* **2010,** *132*, 1738-1739.
23. Zubiria-Ulacia, M.; Matxain, J. M.; Casanova, D., *Phys. Chem. Chem. Phys.* **2020,** *22*, 15908-15918.
24. Hestand, N. J.; Spano, F. C., *Chem. Rev.* **2018**.
25. Hestand, N. J.; Spano, F. C., *Acc. Chem. Res.* **2017,** *50*, 341-350.
26. Grimme, S., *Angew. Chem. Int. Ed.* **2008,** *47*, 3430-3434.
27. Hunter, C. A.; Sanders, J. K. M., *J. Am. Chem. Soc.* **1990,** *112*, 5525-5534.
28. Cozzi, F.; Ponzini, F.; Annunziata, R.; Cinquini, M.; Siegel, J. S., *Angewandte Chemie International Edition in English* **1995,** *34*, 1019-1020.
29. Salonen, L. M.; Ellermann, M.; Diederich, F., *Angew. Chem. Int. Ed.* **2011,** *50*, 4808-4842.
30. Hoeben, F. J. M.; Jonkheijm, P.; Meijer, E. W.; Schenning, A. P. H. J., *Chem. Rev.* **2005,** *105*, 1491-1546.
31. De Greef, T. F. A.; Smulders, M. M. J.; Wolffs, M.; Schenning, A. P. H. J.; Sijbesma, R. P.; Meijer, E. W., *Chem. Rev.* **2009,** *109*, 5687-5754.
32. Liu, C.; Liu, K.; Mukhopadhyay, A.; Paulino, V.; Bernard, B.; Olivier, J.-H., *Organometallics* **2020,** *39*, 2984-2990.
33. Liu, C.; Liu, K.; Klütke, J.; Ashcraft, A.; Steefel, S.; Olivier, J.-H., *J. Mater. Chem. C* **2018,** *6*, 11980-11991.
34. Korevaar, P. A.; George, S. J.; Markvoort, A. J.; Smulders, M. M. J.; Hilbers, P. A. J.; Schenning, A. P. H. J.; De Greef, T. F. A.; Meijer, E. W., *Nature* **2012,** *481*, 492-497.
35. Korevaar, P. A.; de Greef, T. F. A.; Meijer, E. W., *Chem. Mater.* **2014,** *26*, 576-586.
36. Haedler, A. T.; Meskers, S. C. J.; Zha, R. H.; Kivala, M.; Schmidt, H.-W.; Meijer, E. W., *J. Am. Chem. Soc.* **2016,** *138*, 10539-10545.
37. Fukui, T.; Kawai, S.; Fujinuma, S.; Matsushita, Y.; Yasuda, T.; Sakurai, T.; Seki, S.; Takeuchi, M.; Sugiyasu, K., *Nat. Chem.* **2016,** *9*, 493-499.
38. Aliprandi, A.; Mauro, M.; De Cola, L., *Nat. Chem.* **2015,** *8*, 10.
39. Ogi, S.; Grzeszkiewicz, C.; Wurthner, F., *Chem. Sci.* **2018,** *9*, 2768-2773.

40. Mabesoone, M. F. J.; Markvoort, A. J.; Banno, M.; Yamaguchi, T.; Helmich, F.; Naito, Y.; Yashima, E.; Palmans, A. R. A.; Meijer, E. W., *J. Am. Chem. Soc.* **2018,** *140*, 7810-7819.

41. Fennel, F.; Wolter, S.; Xie, Z.; Plötz, P.-A.; Kühn, O.; Würthner, F.; Lochbrunner, S., *J. Am. Chem. Soc.* **2013,** *135*, 18722-18725.

42. Leira-Iglesias, J.; Sorrenti, A.; Sato, A.; Dunne, P. A.; Hermans, T. M., *Chem. Commun.* **2016,** *52*, 9009-9012.

43. Liu, K.; Mukhopadhyay, A.; Ashcraft, A.; Liu, C.; Levy, A.; Blackwelder, P.; Olivier, J.-H., *Chem. Commun.* **2019,** *55*, 5603-5606.

44. Liu, K.; Levy, A.; Liu, C.; Olivier, J.-H., *Chem. Mater.* **2018,** *30*, 2143-2150.

45. Görl, D.; Zhang, X.; Würthner, F., *Angew. Chem. Int. Ed.* **2012,** *51*, 6328-6348.

46. Ashcraft, A.; Liu, K.; Mukhopadhyay, A.; Paulino, V.; Liu, C.; Bernard, B.; Husainy, D.; Phan, T.; Olivier, J.-H., *Angew. Chem. Int. Ed.* **2020,** *59*, 7487-7493.

47. Würthner, F.; Thalacker, C.; Diele, S.; Tschierske, C., *Chem. Eur. J.* **2001,** *7*, 2245-2253.

48. Korevaar, P. A.; Schaefer, C.; de Greef, T. F. A.; Meijer, E. W., *J. Am. Chem. Soc.* **2012,** *134*, 13482-13491.

49. Appel, R.; Fuchs, J.; Tyrrell, S. M.; Korevaar, P. A.; Stuart, M. C. A.; Voets, I. K.; Schönhoff, M.; Besenius, P., *Chem. Eur. J.* **2015,** *21*, 19257-19264.

50. Smulders, M. M. J.; Nieuwenhuizen, M. M. L.; de Greef, T. F. A.; van der Schoot, P.; Schenning, A. P. H. J.; Meijer, E. W., *Chem. Eur. J.* **2010,** *16*, 362-367.

51. Lee, S. K.; Zu, Y.; Herrmann, A.; Geerts, Y.; Müllen, K.; Bard, A. J., *J. Am. Chem. Soc.* **1999,** *121*, 3513-3520.

52. Marcon, R. O.; Brochsztain, S., *J. Phys. Chem. A* **2009,** *113*, 1747-1752.

53. Miller, L. L.; Mann, K. R., *Acc. Chem. Res.* **1996,** *29*, 417-423.

54. Miller, L. L.; Zhong, C. J.; Kasai, P., *J. Am. Chem. Soc.* **1993,** *115*, 5982-5990.

55. Zhong, C. J.; Kwan, W. S. V.; Miller, L. L., *Chem. Mater.* **1992,** *4*, 1423-1428.

56. Spano, F. C.; Silva, C., *Annu. Rev. Phys. Chem.* **2014,** *65*, 477-500.

57. Clark, J.; Chang, J.-F.; Spano, F. C.; Friend, R. H.; Silva, C., *Appl. Phys. Lett.* **2009,** *94*, 163306.

58. Bentea, L.; Watzky, M. A.; Finke, R. G., *J. Phys. Chem. C* **2017,** *121*, 5302-5312.

59. Morris, A. M.; Watzky, M. A.; Finke, R. G., *Biochimica et Biophysica Acta (BBA) - Proteins and Proteomics* **2009,** *1794*, 375-397.

60. Watzky, M. A.; Finke, R. G., *J. Am. Chem. Soc.* **1997,** *119*, 10382-10400.

61. Morris, A. M.; Watzky, M. A.; Agar, J. N.; Finke, R. G., *Biochemistry* **2008,** *47*, 2413-2427.

62. Maka, V. K.; Mukhopadhyay, A.; Savitha, G.; Moorthy, J. N., *Nanoscale* **2018,** *10*, 22389-22399.

63. Mukhopadhyay, A.; Maka, V. K.; Savitha, G.; Moorthy, J. N., *Chem* **2018,** *4*, 1059-1079.

64. Bunck, D. N.; Dichtel, W. R., *J. Am. Chem. Soc.* **2013,** *135*, 14952-14955.

65. Ding, Y.; Chen, Y.-P.; Zhang, X.; Chen, L.; Dong, Z.; Jiang, H.-L.; Xu, H.; Zhou, H.-C., *J. Am. Chem. Soc.* **2017,** *139*, 9136-9139.

66. Berlanga, I.; Ruiz-González, M. L.; González-Calbet, J. M.; Fierro, J. L. G.; Mas-Ballesté, R.; Zamora, F., *Small* **2011,** *7*, 1207-1211.

67. Ardoña, H. A. M.; Draper, E. R.; Citossi, F.; Wallace, M.; Serpell, L. C.; Adams, D. J.; Tovar, J. D., *J. Am. Chem. Soc.* **2017,** *139*, 8685-8692.

68. Kaufmann, C.; Kim, W.; Nowak-Król, A.; Hong, Y.; Kim, D.; Würthner, F., *J. Am. Chem. Soc.* **2018,** *140*, 4253-4258.

69. Mei, J.; Graham, K. R.; Stalder, R.; Tiwari, S. P.; Cheun, H.; Shim, J.; Yoshio, M.; Nuckolls, C.; Kippelen, B.; Castellano, R. K.; Reynolds, J. R., *Chem. Mater.* **2011,** *23*, 2285-2288.

Journal Name

ARTICLE

TOC

Redox-assisted assembly offers new avenues to optimize the excitonic properties and solid-state morphologies of water-soluble perylene bisimide supramolecular polymers